Geodesy and Geodynamics 17 (2026) 391–399

Contents lists available at ScienceDirect

Geodesy and Geodynamics

journal homepage: http://www.keaipublishing.com/geog

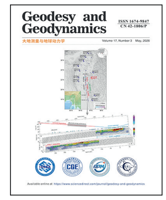

Research Paper

Seismological study of meta-instability of the Yangbi M_S6.4 earthquake in 2021

Shouyong Li

Handan Central Seismic Station, Handan 056001, China

ARTICLE INFO

Article history:
Received 6 April 2025
Received in revised form
7 July 2025
Accepted 17 July 2025
Available online 11 November 2025

Keywords:
Meta-instability
Stress field
Gradient
Gradient divergence
Synergism

ABSTRACT

Meta-instability is an irreversible precursor of earthquakes. To identify the meta-instability precursor of the Yangbi M_S6.4 earthquake (99.87°E, 25.67°N) that occurred on May 21, 2021, we selected seismic data from the pre-earthquake period between May 1 and May 21. We calculated the apparent velocity ratio and the apparent Poisson's ratio within the region (98.5°E−101°E, 24.6°N-27.1°N) and interpolated these values. Our findings revealed that the trends of the fitted straight lines at the maximum and minimum points of the gradient divergences of the apparent velocity ratio field and apparent Poisson's ratio field are consistent with the trend of nodal planes 1 and 2 of the focal mechanism, respectively. Interestingly, the trend of the fitted straight lines at the minimum and maximum points of their values is consistent with the trend of nodal planes 1 and 2 of the focal mechanism, too. Positive gradient divergence values indicate energy released, while negative values suggest energy absorption. This phenomenon is characterized by synergy and can be mutually explanatory. The observed stress state matches the experimentally demonstrated meta-instable state, indicating that it is a precursor signal. We propose that this method can be a reference for identifying the meta-instability of strike-slip strong earthquakes with a significant number of foreshocks. For seismically active regions, increasing the number of stations with rich data acquisition will facilitate more convenient stress field analysis.

1. Introduction

Earthquakes result from stress field movements, making it crucial to closely monitor the stability of crustal media under stress field influence. During stress field movement, the crust exhibits four states: steady, meta-stable, meta-instable, and unstable. Ma et al. conducted an in-depth analysis of these states through experiments, identifying meta-instability as an irreversible precursor to earthquake rupture and providing criteria for its identification [1,2]. This stage is characterized by rich precursor activity, which is significant for capturing earthquake precursors and studying earthquake prediction. To apply meta-instability theory to field observations, researchers have explored its characteristics from various perspectives, including water level [3], deformation [3,4], gravity [5], and temperature [6,7]. These studies have been expressed to some extent. Although meta-instability is a critical state before fault ruptures under stress field influence, describing it from the stress field perspective may have a direct and manifest effect. However, the stress field faces the challenge of being invisible and intangible. Despite this, researchers have proposed a novel method: using other physical quantities to reflect stress field changes. Liu and Lai [8] discovered that abnormal wave velocity is primarily influenced by stress factors and fault structures through experiments, providing a potential method for stress field research. Assuming the medium remains stable, wave velocity can be regarded as a direct indicator of stress field changes. Moreover, the relative stability of Earth's tectonic pattern provides feasibility [9] for using seismic wave velocity to reflect the stress field. Although the discontinuity of observation points and the irregular distribution of epicenters pose challenges, interpolation techniques can effectively approximate the properties of the medium at the interpolation point. Therefore, the stress field can be analyzed from the perspective of field theory. Thus, the relationship between seismic wave velocity and stress field, combined with interpolation methods, is a robust approach to observe stress field changes and thereby study the meta-instability states.

On May 21, 2021, at 21:48:34, an M_S6.4 earthquake occurred in Yangbi, Yunnan Province (99.87°E, 25.67° N). The abundance of

E-mail addresses: 13111330986@163.com, lishy@sina.com.

Peer review under the responsibility of Editorial office of Geodesy and Geodynamics.

https://doi.org/10.1016/j.geog.2025.07.002

foreshocks and the fact that the fault of this earthquake is a shallow strike-slip rupture fault [10–12] provide favorable conditions for capturing meta-instability information. As a retrospective study, we utilized seismological data to calculate the apparent velocity ratio and apparent Poisson's ratio, which are related to seismic wave velocity. We then performed interpolation to achieve grid continuity in the region. The gradient and gradient divergence were used to reflect stress field changes, combined with the distribution characteristics of their contour lines, revealing the morphological changes of the stress field before the earthquake and their intrinsic connections. We aimed to capture meta-instability stages and identify precursor information in field observations, thereby providing references for earthquake prediction.

2. Geologic background

The M_S6.4 earthquakes in Yangbi, Yunnan, occurred on the Yunnan-Burma Block, where the main active framework was formed by the compression of the southeastern margin of the Qinghai-Xizang Plateau. This compression results from the northward subduction of the Indian Plate beneath the Eurasian Plate [13–15]. The western boundary of this block is the arc-shaped subduction zone of Myanmar, while its eastern boundary is the Jinshajiang-Honghe Fault Zone [14]. Since the Cenozoic era, particularly during the late Quaternary period, tectonic activity has been very intense. Fig. 1(a) shows its geographical distribution, with the study area indicated by green squares. There are multiple fault zones in the region, clustering of which may reflect the historical activity patterns of stress fields and earthquake distribution. Fig. 1(b) shows the distribution of these fault zones, with fault zone data sourced from the Deng et al. [16].

Weixi-Qiaohou Fault Zone: Starting from Tongxun and extending to Qiaohou, the fault zone trends 20°N-30°W. The southern segment dips to the northeast with a dip angle of about 50° and has a length of approximately 280 km [17]. Since the early Cenozoic, the fault has exhibited right-lateral strike-slip characteristics, which transformed into a left-lateral strike-slip feature by the Pliocene [18–20].

Chenghai Fault Zone: Formed during the Sinian Period, it is approximately 200 km long. Multiple graben basins have been formed along the fault zone, and the fault nature is characterized by left-lateral strike-slip with normal faulting [21,22].

Honghe Fault Zone: Originating in Eryuan, northern Yunnan Province, it extends southeastward and enters Vietnam near Hekou. The total length is approximately 1000 km, with about 600 km within Yunnan Province. The northern segment exhibits kinematic partitioning between strike-slip and dip-slip motions [21,23]. Since the early Quaternary, large-scale right-lateral strike-slip movements have occurred, and the canyon section is primarily characterized by right-lateral movements [22,24].

Lijiang-Xiaojinhe Fault Zone: Located in the northwestern plateau of Yunnan, the fault trends 40° north of east, has a total length of approximately 360 km, and is a high-angle reverse left-lateral strike-slip active fault [25–27].

Longpan-Qiaohou Fault Zone: Starting in the north from Longpan and extending to Qiaohou in the south, the fault has a total length of approximately 120 km. It was initially characterized

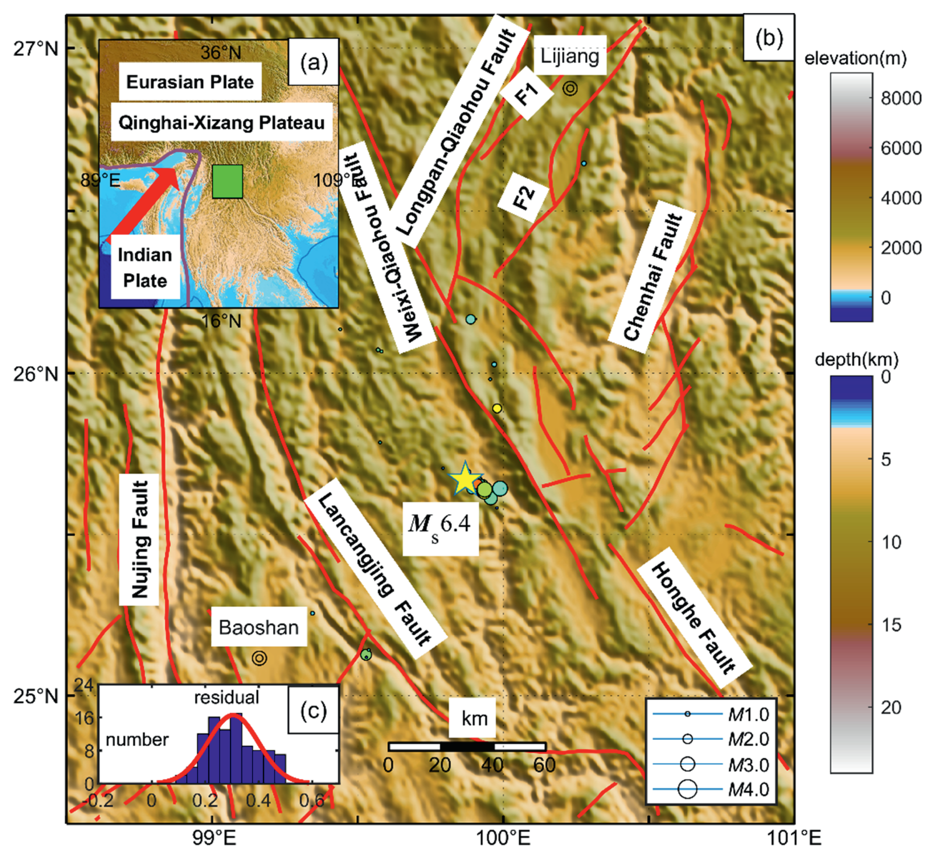

F1：Lijing-Xiaojinghe Fault；F2：Eryuan-Heqing Fault.

Fig. 1. (a) Regional location map. The plate boundary data are from the literature [32]. The green square indicates the study area; (b) The epicenter distribution map, the yellow star indicates the epicenter position of the M_S6.4 earthquake, same for the following figures; (c) Histogram of residuals.

by thrust faulting and later shifted to a left-lateral strike-slip movement nature after the Tertiary Period [21,28].

Eryuan-Heqing Fault Zone: The northern terminus begins at Xiaojinhe Fault, and it forms an arc-shaped structure near Eryuan. Some northeast-trending faults extend southeastward, with left-lateral strike-slip motion and lateral extension being two prominent characteristics [21,29].

Lancangjiang Fault Zone: Distributed along the west side of the Lancang River, starting in the north from Chongshan, it extends southward through Damenglong into Myanmar. Since the Quaternary Period, it has primarily exhibited right-lateral strike-slip characteristics [30].

Nujiang Fault Zone: This fault zone spans approximately 500 km in the western Yunnan Province. As the fault arcs southward, the dip angle of the fault plane decreases while the plunge angle of the stretching lineation increases. The northeast-trending segment exhibits characteristics of both strike-slip motion and thrusting [31].

3. Method and Rationale

3.1. Method

The meta-instability stage is the period during which strain energy accumulates to the ultimate strength of the rack under the action of the stress field until fault rupture occurs, and it is also the most active stage of earthquake precursors. Therefore, from the perspective of the stress field, it should be the most direct method for identifying meta-instability and discovering precursors. In the stress field, the gradient of stress factors indicates the direction of the fastest stress change, which can reflect the direction and magnitude of stress. The gradient divergence represents the rate of change in the density of the stress line, which can reflect the intensity of the stress field activity. Since the stress field is invisible, visualizing these two factors is primary in stress field research. According to the experiment on the relationship between seismic wave velocity and stress factors [8], when the influence of small earthquakes on the stress field is not considered, the stress field is stable. That is, the occurrence of small earthquakes does not affect the trend of stress convergence and divergence at that location. Thus, the changes in the stress field correspond one-to-one with changes in seismic wave velocity. This means that on a “stress field line”, there must be a unique “P-wave velocity line” and a unique “S-wave velocity line”, as well as a unique “velocity ratio line” and a unique “Poisson's ratio line”, all of which have a spatial distribution similar to that of the stress field. Similarly, their gradients can reflect the direction and magnitude of stress, and the divergence of gradients can reflect changes in the intensity of the stress field. Due to the inaccessible nature of the Earth's crust, stations cannot directly measure seismic wave velocities. Therefore, apparent P-wave velocity, apparent S-wave velocity, apparent velocity ratio, and apparent Poisson's ratio can be measured to reflect the stress field. To conduct stress field visualization, observations at the vertical position of the epicenter on the surface are taken as the research data. To give the observed quantities characteristics of a field, interpolation is performed to achieve numerical grid continuity. When the stress field is orthogonal to the surface, the gradient and gradient divergence of these quantities can effectively reflect changes in the direction, magnitude, and intensity of the stress field within the seismic depth range. Considering the complexity of the rock medium, only the direction and intensity of the stress field are considered here, without involving the magnitude. Therefore, analyzing their characteristics is a feasible method for identifying meta-instability and discovering precursor information.

3.2. Calculation

Apparent P-wave velocity and S-wave velocity are two important seismological parameters for studying earthquakes and crustal media. However, their calculation involves the depth of the earthquake source, which exhibits significant systematic uncertainties. To eliminate the influence of this error, the apparent velocity ratio and apparent Poisson's ratio are used for research. As the calculation of apparent velocity ratio and apparent Poisson's ratio involves apparent P-wave velocity and apparent S-wave velocity, the formulas for calculating apparent P-wave velocity, apparent S-wave velocity, apparent velocity ratio, and apparent Poisson's ratio [33] are all provided here:

$$v_{\text{apparentp}} = \frac{l}{t_{\text{pd}} - t_{\text{o}}}. \tag{1}$$

$$v_{\text{apparents}} = \frac{l}{t_{\text{sd}} - t_{\text{o}}}. \tag{2}$$

$$r = \frac{v_{\text{apparentp}}}{v_{\text{apparents}}} = \frac{\frac{l}{t_{\text{pd}} - t_{\text{o}}}}{\frac{l}{t_{\text{sd}} - t_{\text{o}}}} = \frac{t_{\text{sd}} - t_{\text{o}}}{t_{\text{pd}} - t_{\text{o}}}. \tag{3}$$

$$\gamma = 0.5\left(1 - \frac{1}{r^2 - 1}\right) = 0.5\left(\frac{v^2{}_{\text{apparentp}} - 2v^2{}_{\text{apparents}}}{v^2{}_{\text{apparentp}} - v^2{}_{\text{apparents}}}\right). \tag{4}$$

where l represents the focal distance, t_{pd} represents the arrival time of the P-wave, t_{o} represents the time of the earthquake, t_{sd} represents the arrival time of the S-wave, r represents the apparent velocity ratio, and γ represents the apparent Poisson's ratio.

The region is divided into a grid, with grid points determined by the epicenter locations. The average or median values of the apparent velocity ratio and apparent Poisson's ratio within the same grid are taken as the equivalent values for that grid. Then, interpolation is performed to form continuous grid values within the region, endowing it with the characteristics of a field.

3.3. Direction and intensity of stress field

The gradient indicates the direction of the fastest change in the apparent velocity ratio or apparent Poisson's ratio within the field, forming a vector field. The divergence of the gradient quantifies the rate of change in the gradient density per unit area within the field. The calculation of the gradient is shown in Eq. (5), where $\boldsymbol{i}$ and $\boldsymbol{j}$ represent unit vectors. Let the vector field of the gradient be denoted $\boldsymbol{A} = p(x,y)\boldsymbol{i} + q(x,y)\boldsymbol{j}$ and then its divergence is calculated as shown in Eq. (6) [34].

$$\textbf{grad}f = \frac{\partial f}{\partial x}\boldsymbol{i} + \frac{\partial f}{\partial y}\boldsymbol{j}. \tag{5}$$

$$\textbf{div}\boldsymbol{A} = \frac{\partial p}{\partial x} + \frac{\partial q}{\partial y}. \tag{6}$$

A high field density indicates a high field intensity, while a decrease in field density indicates flux outflow. Conversely, an increase in field density indicates flux inflow. Flux, by definition, can be represented as the energy transfer per unit area in the gradient direction over a specified time interval. The gradient divergence serves as a measure of the change in the gradient field intensity. A positive divergence value signifies a high field intensity characterized by energy radiating outward; a negative divergence value indicates a weak field intensity with energy converging from the surroundings. The direction of the gradient is the fastest route from regions of lower density to those of higher density, indicating the direction of energy flow, which aligns with the direction of stress (the length of the arrow can reflect the magnitude of the stress). When the stress field is orthogonal to the surface, the gradient and its divergence can effectively reflect the direction and intensity of the stress field.

4. Data and results

4.1. Selection and processing of data

The period from May 1 to 21, 2021, which is the pre-seismic phase, represents a relatively independent interval of concentrated minor seismic activity; therefore, the data collected during this time frame were selected as the focus study. This study used the observation reports from China Earthquake Networks Center as the fundamental data. Seismic data within the range of 98.5°E−101.0°E and 24.6°N-27.1°N are selected. Aiming to process equivalent properties near the epicenter, we selected data with epicentral distances ranging from 20 km to 100 km to ensure clear seismic phases. To ensure that the calculated data were near the epicenter, we chose earthquakes with Pg and Sg wave records in all four quadrants around the epicenter. To ensure the accuracy of the location, we selected earthquakes with location residuals less than 0.5. A total of 100 earthquakes met these criteria, with an average residual value of 0.3029. The epicentral distribution and residual histogram are shown in Fig. 1(b) and (c), respectively. For these data, we calculated the apparent velocity ratio and apparent Poisson's ratio. To eliminate noise and stabilize the interpolated data, the study area was divided into a $10' \times 10'$ grid. For grids containing multiple epicenters, the median values of the apparent velocity ratio and apparent Poisson's ratio were used as the representative values for those grids. For grids with only one earthquake, the calculated values of the apparent velocity ratio and apparent Poisson's ratio were used as the representative values. Considering: (i) the advantages of spline interpolation in smoothness and stability; (ii) the continuous and differentiable properties of crustal media at a specified scale; and (iii) the uneven distribution of epicenters, we chose the adjustable tension continuous curvature spline interpolation method, with the tension factor set to 0.2 [35]. We refined the data with a $1' \times 1'$ grid to ensure the continuity of grid values across the entire area, and endowed it with the characteristics of a field. To clearly represent the gradient, we selected a $4' \times 4'$ grid.

The standard deviation of the apparent velocity ratio and the residual after grid interpolation are shown in Fig. 2 (a) and (b), respectively. The standard deviation of the apparent Poisson's ratio and the residual after grid interpolation are shown in Fig. 2 (c) and (d), respectively. Since in light of the lack of seismotectonic evidence for deep-crust fault structures within the study area, the data quality and processing methods are considered reliable.

4.2. Apparent velocity ratio field

The contour lines of the apparent velocity ratio field are shown in Fig. 3 (a), with minimum points A (99.56°E, 26.05°N) and B (99.84°E, 25.70°N). The distance between them is 48.6 km, and the trend of the fitted line a is 142.8°. The maximum points are C (100.27°E, 26.66°N), D (99.87°E, 26.17°N), E (99.55°E, 25.76°N), and F (99.20°E, 25.42°N), with the trend of the fitted line b being 40.5°. The gradient and its divergence are shown in Fig. 3 (b). The gradients reflect the direction of the stress field, while the gradient divergence indicates the degree of change in the stress field intensity. The maximum divergence points are A′ (99.60°E, 26.10°N) and B′ (99.88°E, 25.74°N), with a distance of 49.1 km between them and a trend of 141.8° for the fitted line a′. The minimum divergence points are C′ (100.30°E, 26.59°N), D′ (99.98°E, 26.11°N), E′ (99.58°E, 25.79°N), and F′ (99.30° E, 25.30° N), with the trend of 39.1° for the fitted line b′.

4.3. Apparent Poisson's ratio field

The contour lines of the apparent Poisson's ratio field are shown in Fig. 4 (a), with the minimum points being A (99.58°E, 26.05°N) and B (99.84°E, 25.70°N). The distance between them is 46.9 km, and the trend of the fitted line a is 143.9°. The maximum points are C (100.28°E, 26.65°N), D (99.88°E, 26.16°N), and E (99.32°E, 25.25°N), with the trend of the fitted line b being 34.2°. The gradient and its divergence are shown in Fig. 4 (b). The gradients reflect the direction of the stress field, while the gradient divergence indicates the degree of change in the stress field intensity. The maximum divergence points are A′ (99.60°E, 26.10°N) and B′ (99.87°E, 25.73°N), with a distance of 49.9 km between them and a trend of 144.0° for the fitted line a′. The minimum divergence points are C′ (100.29°E, 26.60°N), D′ (99.98°E, 26.12°N), E′ (99.59°E, 25.79°N), and F′ (99.27°E, 25.48°N), with the trend of 49.9° for the fitted line b′.

The above results reveal a correlation between the extremum points of the apparent velocity ratio field and the apparent Poisson's ratio field and their corresponding gradient divergence extremum points. Specifically, the minimum points of the apparent velocity ratio and apparent Poisson's ratio fields correspond to the maximum gradient divergence points, while the maximum points correspond to the minimum gradient divergence points.

5. Discussion

5.1. Analysis of the apparent velocity ratio field

Fig. 3 (a) shows the contour distribution of the apparent velocity ratio field, highlighting minimum value points A and B, as well as maximum value points C, D, E, and F. Fig. 3 (b) shows the variation of the gradient and gradient divergence of the apparent velocity ratio field, the maximum points A′ and B′ indicate energy release, while the minimum points C′, D′, E′, and F′ indicate energy absorption. The characteristics exhibited by points A′, B′, C′, D′, E′, and F′ are consistent with the energy activity pattern during the meta-instability stage, reflecting a certain degree of fault synergism [1,2,36]. These points show the activity traces of the fault. According to the literatures [37,38], the release of energy by the rock medium leads to a decrease in temperature, while the absorption of energy causes an increase in temperature. Temperature changes have a highly sensitive effect on velocity ratio [39]. When the temperature decreases, the velocity ratio rapidly decreases, and as the temperature increases, the velocity ratio rapidly increases. Experimental have shown that the velocity ratio changes with pressure in four ways: (i) a significant decrease with increasing pressure; (ii) a slow increase with increasing pressure; (iii) a slow decrease with increasing pressure; and (iv) a slow fluctuation with increasing pressure [40]. Therefore, it is inferred that the primary determination for velocity ratio changes in the source environment may be the temperature changes of the medium due to energy release or absorption during the stress field variation process. This explains the geographical correspondence between points A, B, C, D, E, and F and points A′, B′, C′, D′, E′, and F′. The absorption of energy leads to an increase in temperature and a significant increase in the apparent velocity ratio field, while the released energy results in a decrease in temperature and a

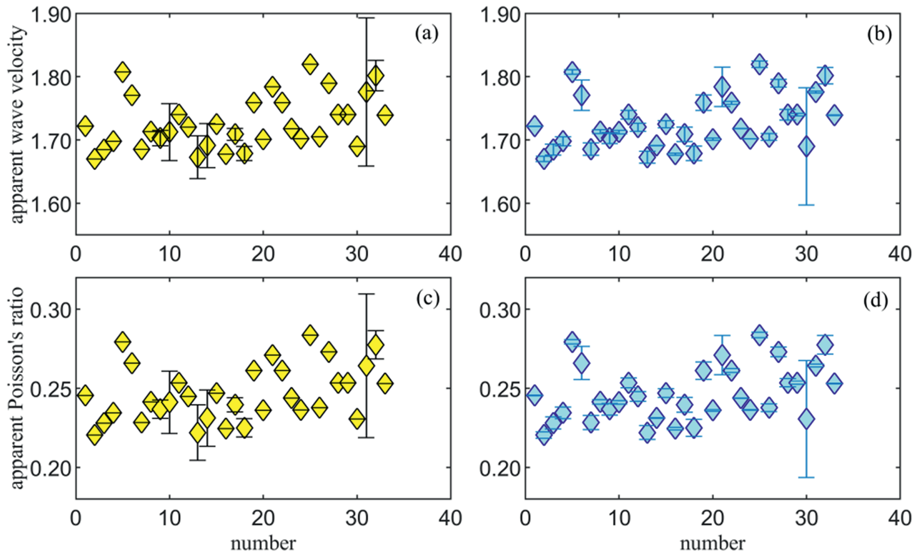

Fig. 2. (a) Standard deviation of the median of the apparent velocity ratio in ten equal parts of the grid; (b) Residuals after interpolation of the apparent velocity ratio; (c) Standard deviation of the median of the apparent Poisson's ratio in ten equal parts of the grid; (d) Residuals after interpolation of the apparent Poisson's ratio.

significant decrease in the apparent velocity ratio field. The distance between the minimum points A and B in Fig. 3 (a) is 48.6 km, with a fitted line trend of 142.8°. The distance between the maximum points A′ and B′ in Fig. 3 (b) is 49.1 km, trending 141.8°. The fitted line trend for the maximum points C, D, E, and F in Fig. 3 (a) is 40.5°, while the trend for the minimum points C′, D′, E′, and F′ in Fig. 3 (b) is 39.1°. Although Fig. 3 (a) and (b) represent two different physical fields, they are essentially the same and can be mutually explanatory. Both are manifestations of energy release and absorption on a locked fault during the meta-instability stage, with Fig. 3 (a) showing characteristics indirectly induced.

5.2. Analysis of the apparent Poisson's ratio field

Fig. 4 (a) shows the contour distribution of the apparent Poisson's ratio field, highlighting minimum value points A and B, as well as maximum value points C, D, and E. Fig. 4 (b) shows the changes in the gradient and gradient divergence of the apparent

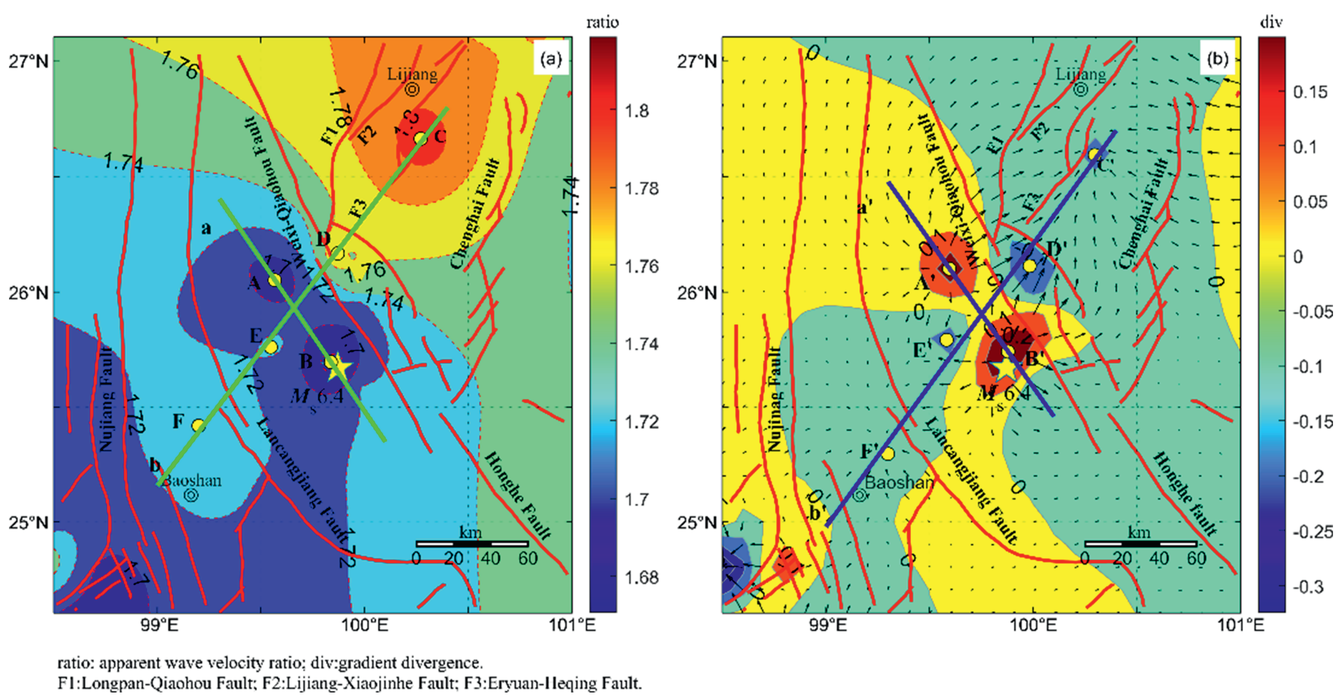

Fig. 3. (a) Distribution map of the contour lines of the apparent velocity ratio field. Points A and B are local minima, while points C, D, E, and F are local maxima. Line a is the fitting line through the local minima, and line b is the fitting line through the local maxima; (b) Distribution map of the gradient and gradient divergence of the apparent velocity ratio field. Points A'and B' are local maxima, while points C′, D′, E′, and F′ are local minima. Line a′ is the fitting line through the local maxima, and line b′ is the fitted line through the local minima.

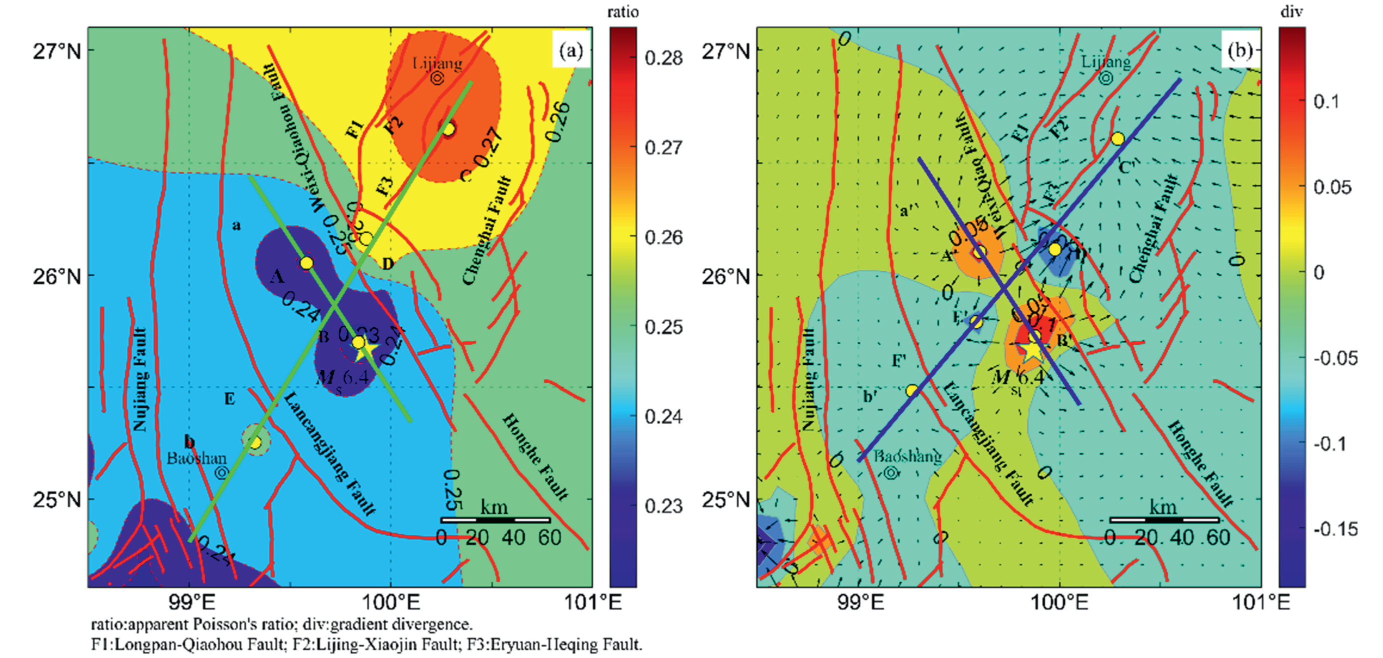

Fig. 4. (a) Distribution map of the contour lines of the apparent Poisson's ratio field. Points A and B are local minima, while points C, D, and E are local maxima. Line a is the fitting line through the local minima, and line b is the fitting line through the local maxima; (b) Distribution map of the gradient and gradient divergence of the apparent Poisson's field. Points A′ and B′ are local maxima, while points C′, D′ and E′ are local minima. Line a′ is the fitting line through the local maxima and line b′ is the fitting line through the local minima.

Poisson's ratio field. The maximum points A′ and B′ indicate energy release, while the minimum points C′, D′, E′, and F′ indicate energy absorption. The characteristics reflected by A′, B′, C′, D′, E′, and F′ are consistent with the activity traces of the fault, indicating a certain degree of fault synergism. The energy activity patterns are also consistent with the characteristics of the meta-instability stage [1,2,36]. According to the literatures [41,42], changes in Poisson's ratio, similar to the velocity ratio, are highly sensitive to temperature changes. When the temperature decreases, the Poisson's ratio rapidly decreases, and as the temperature increases, the Poisson's ratio rapidly increases. After reaching a certain level of confining pressure, the Poisson's ratio will not change significantly with further increases in confining pressure. Similar to the apparent velocity ratio field, it is inferred that the primary changes in the apparent Poisson's ratio field may also be temperature changes in the medium due to energy or absorption. This explains the geographical correspondence between points A, B, C, D, and E and points A′, B′, C′, D′, E′, and F′. The absorption of energy leads to an increase in temperature and a significant increase in the apparent Poisson's ratio field, while the release of energy results in a decrease in temperature and a significant pronounced diminution in the apparent Poisson's ratio field. In Fig. 4 (a), the distance between the minimum points A and B is 46.9 km, with a fitted line trend of 143.9°. In Fig. 4 (b), the distance between the maximum points A′ and B′ is 49.9 km, trending 144.0°. The fitted line trend for the maximum points C, D, and E in Fig. 4 (a) is 34.2°, while the trend for the minimum points C′, D′, E′, and F′ in Fig. 4 (b) is 49.9°. The geographical differences between these points are numerically larger, which is believed to be due to the concentration of energy release and the broader range of energy absorption, as well as mismatches in complex media conditions, such as thermal conductivity and the rate of energy release. Although Fig. 4 (a) and (b) represent two different physical fields, they are essentially the same and can be mutually explanatory. Both are manifestations of energy release and absorption on the locked fault during the meta-instability stage, with Fig. 4 (a) showing characteristics indirectly induced.

5.3. Relationship

The contour lines of the apparent velocity ratio field and apparent Poisson's ratio field, as well as the divergence diagrams of their gradients, all reflect the same issue: the state of the stress field near the fault when the earthquake occurs. The trend of the fitted line for the minimum points of the apparent velocity ratio field (142.8°) and the trend of the fitted line for the maximum points of its gradient divergence field (141.8°), as well as the trend of the fitted line for the minimum points of the apparent Poisson's ratio field (143.9°) and the trend of the fitted line for the maximum points of its gradient divergence (144.0°), are consistent with the trend of the node 1(138°) of the focal mechanism solution for this earthquake in the CMT catalog of China Earthquake Networks Center [43]. The trend of the fitted line for the maximum points of the apparent velocity ratio field (40.1°) and the trend of the fitted line for the minimum points of its gradient divergence (39.1°), as well as the trend of the fitted line for the maximum points of the apparent Poisson's ratio field (34.2°) and the trend of the fitted line for the minimum points of its gradient divergence (49.9°), are consistent with the trend of node 2 (45°) (although there are some differences, they are considered to be within an acceptable range). This fully illustrates their precursor property, that is, the state of the stress field before the fault instability and rupture. The energy absorption and release reflected by the gradient divergence are consistent and unified with the changes in the apparent velocity ratio field and apparent Poisson's ratio field values caused by the temperature changes in the medium due to this process. Since earthquakes are a phenomenon of energy released by fault rupture, and their brewing process results from the overall stress field movement in the region, local data anomalies do not have complete precursor significance. Anomalies in several diverse data domains, lacking an organic connection, may also fail to make functional judgments on precursors. Instead, the movement of the stress field should be viewed as a whole to assess the stress state and distinctly differentiate the precursors. The geographical distribution of locked faults can be estimated based on the extreme energy release loci's spatial uncertainties. The specific epicenter location may be affected by the constantly changing geophysical environment on the locked fault. From an energy perspective, areas with elevated strain energy dissipation rates are kinetically predominant to become stick-slip transition and rupture points.

Based on the above analysis, the possible process of this earthquake is inferred as follows. In the interaction between the tectonic blocks, the stress field, influenced by the fault zones within the region, accumulates energy on the locked fault. When the strain energy on the locked fault accumulates to the limit that the rock can withstand, it activates the locked fault, entering the irreversible meta-instability stage of rupture. The locked fault transitions from a state primarily energy-absorbing to one energy-releasing. As energy is released from the locked fault and absorbed by its conjugate plane, the energy conversion becomes increasingly intense. As it further develops and reaches a certain degree of synergism, the extreme points of energy release show signs of activity on the locked fault. Simultaneously, the rock medium experiences temperature decreases and increases with energy release and absorption, resulting in minimum and maximum values of the velocity ratio field and Poisson's ratio field (the apparent velocity ratio field and apparent Poisson's ratio field also show minimum and maximum values vertically on the ground). As the stress field activity intensifies and the synergism pressure-solution strengthens, the fault ultimately becomes unstable and the earthquake occurs.

Through the above analysis, it is believed that the meta-instability precursor of the Yangbi M_S6.4 earthquake can be understood as the comprehensive physical response of the surrounding medium to the stress field state and energy transport process before the rock medium instability and rupture. This not only aligns with the definition of precursors described in the literature [44], but also validates the relationship between seismic wave velocity, faults, and stress factors as described in experiments. Moreover, it is consistent with the characteristics of different physical fields corroborating each other in meta-instability states [1] and the uniqueness of precursor features. Additionally, although the apparent velocity ratio and apparent Poisson's ratio are affected by the same errors during processing, their non-linear relationship and the consistency of their gradient divergence illustrate the objectivity of their mathematical relationship. Additionally, the consistency between their contours and gradient divergence reflects the uniqueness of seismic precursor features. In field observations, it is believed that this method has definitive reference values for identifying the meta-instability stages and discovering precursors.

5.4. Question and future

The effectiveness of this method essentially depends on the richness of the data and is also limited by the geometric relationship between the observation plane and the stress field. It can effectively reflect the state of the stress field when they are orthogonal. Despite the stringent selection criteria employed for the research dataset, which included earthquakes with well-documented records, precise epicentral locations, and complete seismic phase records in all four quadrants surrounding the epicenter, the processed data are capable of capturing the general characteristics of the regional crustal medium. However, it is important to note that the calculated apparent velocity ratio and apparent Poisson's ratio represent effective approximations specifically at the epicentral locations. Given the inherent complexity and heterogeneity of the crustal medium, local deviations in the data may still exist. In non-orthogonal cases, the vertical projection of the stress field on the ground may become indistinguishable due to overlap. Moreover, the presence of minerals such as oil and gas in the rock medium may cause discontinuities in the stress field, which is another reason why its projection on the ground cannot effectively reflect the state of the stress field, thus posing a challenge to the study of the meta-instability state. Attenuation imaging shows that within the depth range of 20–40 km in this region, there is strong attenuation under the influence of upwelling mantle, characterized by low Q-values, high Poisson's ratio, low velocities, and high electrical conductivity [45,46]. The rupture fault of the Yangbi M_S6.4 earthquake, inferred from coseismic deformation data obtained by synthetic aperture radar interferometry (InSAR), is a shallow strike-slip type with slip mainly distributed between 2 km and 12 km [10]. It is almost unaffected by the aforementioned attenuation features, and it is orthogonal to the stress field. So, its vertical projection on the ground can effectively reflect the state of the stress field. Although the above situation restricts further research on the stress field, since the vertical projection of the stress field on the ground reflects the state of the stress field within the seismic depth range, it is possible to use data with well-constrained seismic depth to obtain detailed dynamic changes of the stress field from different depths in a three-dimensional perspective, providing references for earthquake prediction and disaster prevention.

6. Conclusion

(1) The precursor information of meta-instability is a comprehensive response of the rock medium to the state of the stress field and its associated physical phenomena before fault rupture. Due to the complexity of the rock medium, there may be some differences in the physical forms reflected by different observation methods.
(2) In field observations, data interpolation is an effective method for discovering precursor information, especially in data-sparse areas.
(3) Quantities related to seismic wave velocity can effectively reflect the state of the stress field, and the patterns of their gradients and gradient divergences are consistent.
(4) The identification of the meta-instability stage is extrapolated based on a certain number of high-quality data to ensure the accuracy and reliability of the analysis results.
(5) When the two-dimensional surface plane tends to be orthogonal to the stress field, precursor information of meta-instability is more easily identifiable, although this situation may be affected by the continuity of the underground medium; when not orthogonal, due to the occurrence of projection overlap, surface observation data hardly effectively reflect the state of the stress field, thereby increasing the difficulty of identification.

CRediT authorship contribution statement

Shouyong Li: Writing – review & editing, Writing – original draft, Visualization, Software, Project administration, Formal analysis, Data curation.

Declaration of competing interest

The author declares that there is no conflicts of interest.

Acknowledgements

We gratefully acknowledge the use of Generic Mapping Tools (GMT) [47] and the MATLAB-based M-map [48] toolbox for data processing and visualization throughout this study.

References

[1] J. Ma, 'whether earthquake precursors help for prediction do exist', Chin. Sci. Bull. 61 (4/5) (2016) 409–414, https://doi.org/10.1360/N972015-01239.
[2] J. Ma, S.I. Sherman, Y.S. Guo, Identification of meta-instable stress state based on experimental study of evolution of the temperature field during stick-slip instability on a 5° bending fault, Sci. China Earth Sci. 42 (5) (2012) 633–645, https://doi.org/10.1007/s11430-012-4423-2.
[3] S.L. Zhang, Y. Li, X. Wang, et al., Outdoor observation evidence of the meta-instability state, J. Jilin Univ. (Earth Sci. Ed). 46 (2) (2016) 603–609, https://doi.org/10.13278/j.cnki.jjuese.201602304.
[4] S.L. Zhang, X. Wang, W.F. Guo, H, et al., Sub-instability phenomena in various geophysical fields observation data, J. Jilin Univ. (Sci. Ed.) 51 (2) (2021) 571–583, https://doi.org/10.13278/j.cnki.jjuese.20200032.
[5] S.S. Guo, Y.Q. Zhu, Y.M. Xu, et al., Gravity evidence of meta-instable state before the 2008 Wenchuan earthquake, Seismol. Geol. 43 (6) (2021) 1368–1380, https://doi.org/10.3969/j.issn.0253-4967.2021.06.002.
[6] Y.Q. Ren, Experimental study of evolution of the thermal field in the meta-instability stage of faults and its application to earthquake precursors analysis, Institute of Geology, China Earthquake Administration, Beijing, 2015.
[7] S.Y. Chen, P.X. Liu, L.C. Chen, et al., Evidence from seismological observation for detecting dynamic change in crustal stress by bedrock temperature, Chin. Sci. Bull. 65 (22) (2020) 2395–2405, https://doi.org/10.1360/TB-2020-0089.
[8] X.H. Liu, D.L. Lai, Two factors influencing the anomaly of wave velocities, Acta Seismol. Sin. 8 (1) (1986) 50–56, https://doi.org/10.3969/j.issn.0253-3782.1986.01.008.
[9] J. Ma, Tectonophysical research on fault-block tectonics and earthquakes, Chin. J. Geol. 44 (4) (2009) 1071–1082, https://doi.org/10.3321/j.issn:0563-5020.2009.04.007.
[10] J.Y. Yang, Y.M. Wen, C.J. Xu, The 21 May 2021 *Ms*6.4 Yangbi(Yunnan) earthquake: a shallow strike-slip event rupturing in a blind fault, Chin. J. Geophys. 64 (9) (2021) 3101–3110, https://doi.org/10.6038/cjg2021P0408.
[11] F. Long, Y.P. Qi, G.X. Yi, et al., Relocation of the Ms6.4 Yangbi earthquake sequence on May 21, 2021 in Yunnan Province and its seismogenic structure analysis, Chin. J. Geophys. 64 (8) (2021) 2631–2646, https://doi.org/10.6038/cjg2021O0526.
[12] X.L. Lei, Z.W. Wang, S.L. Ma, et al., A preliminary study on the characteristics and mechanism of the May 2021 Ms6.4 Yangbi earthquake sequence, Yunnan, China, Acta Seismol, Sin 43 (3) (2021) 261–286, https://doi.org/10.6038/cjg2021P0401.
[13] Q.D. Deng, P.Z. Zhang, Y.K. Ran, et al., Basic characteristics of China's activity structure, Sci. China Earth Sci. 32 (12) (2002) 1020–1030, https://doi.org/10.3321/j.issn:1006-9267.2002.12.007.
[14] P.Z. Zhang, Q.D. Deng, G.M. Zhang, et al., Strong earthquake activity and active blocks in Chinese mainland, Sci. China Earth Sci. 33 (z1) (2003) 12–20, https://doi.org/10.3321/j.issn:1006-9267.2003.z1.002.
[15] G.M. Zhang, H.S. Ma, H. Wang, et al., Boundaries between active-tectonic blocks and strong earthquakes in the China mainland, Chin. J. Geophys. 48 (3) (2005) 602–610, https://doi.org/10.3321/j.issn:0001-5733.2005.03.018.
[16] Q.D. Deng, Y.K. Ran, X.P. Yang, et al., Active tectonics map of China, Seismological press, Beijing, 2007.
[17] Z.G. Shao, Analysis on the geodynamics of the Lanping-Weixi field, Yunnan province, China University of Geosciences, Beijing, 2003.
[18] Z.F. Chang, H. Chang, Y. Zang, et al., Recent active features of Weixi-Qiaohou fault and its relationship with the Honghe fault, J. Geom. 22 (3) (2016) 517–530, https://doi.org/10.3969/j.issn.1006-6616.2016.03.009.
[19] Z.F. Chang, H. Chang, J.L. Li, et al., Holocene activity and paleoearthquakes of the Weixi-Qiaohou Fault, Seismol. Geol. 43 (4) (2021) 881–898, https://doi.org/10.3969/j.issn.0253-4967.2021.04.009.
[20] Z.F. Chang, J.L. Li, H. Chang, et al., Late-Quaternary activity of Tongdian-Madeng basin segment of Weixi-Qiaohou fault, Acta Sci. Nat. Univ. Pekin. 58 (5) (2022) 875–887, https://doi.org/10.13209/j.0479-8023.2022.057.
[21] Institute of Geology, China earthquake Administration and Yunnan earthquake agency, active faults in the Northwest Yunnan region, Seismological Press, Beijing, 1990, pp. 106–109.
[22] S.M. Guo, H.F. Xiang, J. Zhang, et al., Discussion on the deformation band and magnitude of the 1515 Yongsheng earthquake in Yunnan province, J. Seismol. Res. 11 (2) (1988) 153–162.
[23] P. Tian, Z.S. Yang, C.J. Yu, et al., Chronological evidence of Cenozoic activity in the middle and southern part of Ailao Mountain-Red River fault zone, GSC 10 (2) (2023) 42–53, https://doi.org/10.19388/j.zgdzdc.2023.02.06.
[24] S.M. Guo, H.F. Xiang, F.J. Ji, et al., A study on the relation between Quaternary right-lateral slip and tip extension along the Honghe fault, Seismol. Geol. 18 (4) (1996) 301–309, https://doi.org/10.3969/j.issn.0253-4967.1996.04.006.
[25] H.F. Xiang, X.W. Xu, S.M. Guo, et al., Sinistral thrusting along the Lijiang-Xiaojinhe fault since Quaternary and its geologic-tectonic significance——Shielding effect of transverse structure of intracontinental active block, Seismol. Geol. 24 (2) (2002) 188–198, https://doi.org/10.3969/j.issn.0253-4967.2002.02.006.
[26] R. Ding, J.J. Ren, S.M. Zhang, et al., Late Quaternary paleoearthquakes on the middle segment of the Lijiang-Xiaojinhe fault, Southeastern Tibet, Seismol. Geol. 40 (3) (2018) 622–640, https://doi.org/10.3969/j.issn.0253-4967.2018.03.009.
[27] Z. Gong, H.B. Li, F.T. Tang, et al., Fault zone scale, fault zone structure and historical activity of the Yanyuan segment of the Lijiang-Xiaojinhe fault, Acta Geol. Sin. 97 (7) (2023) 2111–2125, https://doi.org/10.19762/j.cnki.dizhixuebao.2023129.
[28] Z.F. Chang, H. Zhao, J.L. Li, et al., Geometric structure characteristics of Jiuhe-Xionggu segment of Longpan-Qiaohou fault: tectonic geomorphology and geophysical evidence, J. Yunnan Univ. Nat. Sci. Ed. 45 (S1) (2023) 206–214, https://doi.org/10.7540/j.ynu.2023a30.
[29] Y.G. Fang, W.X. Luo, H. Ye, et al., Late Quaternary activity of Heqing-Eryuan fault and its impact on water diversion project in the central Yunnan, South China, J. Seismol. 39 (3) (2019) 6–13, https://doi.org/10.13512/j.hndz.2019.03.002.
[30] G.X. Li, A preliminapy study of some thrust-nappe structures in Lanping basin, Yunnan Geol. 13 (2) (1994) 203–213.
[31] J.C. Li, Neotectonic feature of the Nujiang fault zone in Western Yunnan, Seismol. Geol. 20 (4) (1988) 312–320, https://doi.org/10.3969/j.issn.0253-4967.1998.04.007.
[32] P. Bird, An updated digital model of plate boundaries, Geochem. Geophys. Geosyst. 4 (3) (2003) 1–52, https://doi.org/10.1029/2001GC000252.
[33] N.I. Christensen, Poisson's ratio and crustal seismology, J. Geophys. Res. 101 (B2) (1996) 3139–3156, https://doi.org/10.1029/95JB03446.
[34] S.Y. Xie, Engineering mathematics——vector analysis and field theory, 36, Higher Education Press, Beijing, 2019, p. 53.
[35] W.H.F. Smith, P. Wessel, Gridding with continuous curvature splines in tension, Geophysics 55 (3) (1990) 293–305, https://doi.org/10.1190/1.1442837.
[36] J. Ma, Y.S. Guo, Accelerated synergism prior to fault instability: evidence from laboratory experiments and an earthquake case, Seismol. Geol. 36 (3) (2014) 547–561, https://doi.org/10.3969/j.issn.0253-4967.2014.03.001.
[37] S.Y. Chen, L.Q. Liu, P.X. Liu, et al., Theoretical and experimental study on relationship between stress-strain and temperature variation, Sci. China Earth Sci. 39 (10) (2009) 1446, https://doi.org/10.1007/s11430-009-0183-z, 1445.
[38] M.D. Deng, N.G. Geng, C.Y. Cui, et al., The study on the variation of thermal state of rocks caused by the variation of stress state of rocks, Earthq. Res. China 13 (2) (1997) 179–185.
[39] D.Y. Feng, Abnormal seismic wave velocity, Seismological Publishing Press, Beijing, 1981, p. 10.
[40] N.G. Geng, J.S. Hao, J.H. Li, et al., The relationship between the wave velocity ratio of rocks and hydrostatic pressure, Acta Seismol. Sin. 14 (4) (1992) 500–506, https://doi.org/10.3321/j.issn:0253-4967.1992.04.004.
[41] S.C. Ji, Q. Wang, S.S. Sun, Seismic properties of crystalline rocks and geological and geophysical implication, Chin. J. Geol. 44 (4) (2009) 1113–1135, https://doi.org/10.3321/j.issn:0563-5020.2009.04.008.
[42] A.G. Chen, Q.T. Lü, J.G. Du, et al., The Poisson's ratio of the crust-mantle of South China and its geological significance, Geol. China 46 (4) (2019) 750–758, https://doi.org/10.12029/gc20190406.
[43] Z.G. Yang, T.R. Xu, J.H. Ling, et al., CMT product catalog of the focal mechanism of China Earthquake networks center, 2022, https://doi.org/10.12080/nedc.11.ds.2022.0005orCSTR:12166.11.ds.2022.0005. https://data.earthquake.cn/datashare/report.shtml?PAGEID=earthquake_dzzyjz. (Accessed 13 October 2024).
[44] Y.T. Chen, Earthquake prediction: retrospect and prospect, Sci. China Earth Sci. 39 (12) (2009) 1633–1658, https://doi.org/10.1360/2009-12001.
[45] X. He, L.F. Zhao, X.B. Xie, et al., Weak crust in Southeast Tibetan Plateau revealed by Lg-Wave attenuation tomography: implications for crustal material escape, JGR:SE 126 (3) (2021), https://doi.org/10.1029/2020JB020748.
[46] R.J. Li, L.F. Zhao, X.B. Xie, et al., Crustal deformation in the southeastern margin of the Tibetan plateau:insights from broad-band Pg-wave attenuation

tomography, Geophys. J. Int. 235 (3) (2023) 2870–2886, https://doi.org/10.1093/gji/ggad404.
[47] P. Wessel, J.F. Luis, The GMT/MATLAB toolbox, Geochem. Geophys. Geosyst. 18 (2) (2017) 811–823, https://doi.org/10.1002/2016GC006723.
[48] M_Map:Users guide v1.4. https://www-old.eoas.ubc.ca/~rich/mapug.html. (Accessed 16 June 2023).

Shouyong Li, male, senior engineer, engaged in seismic monitoring work, mainly focusing on seismic waves and geodynamics.